Polymers for Advanced Technologies

WILEY

polymers for advanced technologies

RESEARCH ARTICLE OPEN ACCESS

Regenerable Magnetic Iron Oxide Incorporated Chitosan Beads for Sulfate (SO_4^{2-}) Removal From Wastewater: Isotherms, Kinetics and Mechanism

Uswa Zahra[1] | Imran Ahmad Khan[1] | Asad Ullah Khan[1] | Muhammad Yasir[2] | Wenjuan Zhang[3] | Kashif Mairaj Deen[4] | Edouard Asselin[4] | Rehan Sadiq[5] | Muhammad Nouman Aslam Khan[1] | Nasir M. Ahmad[1]

[1]Polymer Research Lab, School of Chemical and Materials Engineering (SCME), National University of Sciences and Technology (NUST), Islamabad, Pakistan | [2]Centre of Polymer Systems, University Institute, Tomas Bata University in Zlín, Zlín, Czech Republic | [3]State Key Laboratory of Advanced Metallurgy, University of Science and Technology Beijing, Beijing, China | [4]Department of Materials Engineering, The University of British Columbia, Vancouver, British Columbia, Canada | [5]Department of Civil Engineering, School of Engineering, The University of British Columbia Okanagan Campus, Kelowna, British Columbia, Canada

Correspondence: Muhammad Yasir (yasir@utb.cz) | Nasir M. Ahmad (nasir.ahmad@scme.nust.edu.pk)

Received: 23 July 2025 | **Revised:** 3 October 2025 | **Accepted:** 15 October 2025

Funding: This work was supported by Higher Education Commission, Pakistan (NRPU Project No. 6020), Ministerstvo Životního Prostředí (CZ.10.03.01/00/22_003/0000045), Ministerstvo Školství, Mládeže a Tělovýchovy (CZ.02.01.01/00/23_021/0009004, RP/CPS/2024-28/002).

Keywords: adsorption | chitosan bead | iron oxide | sulfate removal | wastewater treatment

ABSTRACT

Sulfate contamination removal from mine waste and industrial water is a primary environmental concern, with high concentrations leading to disease. This research focuses on the preparation of iron oxide-incorporated chitosan beads (IOICBs) for the effective adsorption removal of sulfate. The IOICBs were synthesized by a chemical co-precipitation approach and characterized by Scanning Electron Microscopy, x-ray Diffraction, Brunauer–Emmett–Teller analysis, Fourier Transform Infrared Spectroscopy, and energy-dispersive x-ray mapping for structural, chemical, and morphological properties. The sulfate adsorption on IOICBs was investigated in batch mode studies using UV–Vis spectroscopy. The effect of several parameters, such as adsorbent dosage, pH, initial concentration, and contact time, on the sorption capacity of the IOICBs was studied. The IOICBs have a high efficacy for sulfate removal from contaminated water at pH 2 with a maximum sorption capacity of 147.7 mg/g at room temperature. The mechanism suggested that the presence of acidic NH_4^+ functional groups on the surface of chitosan facilitates the chemisorption of the sulfate ions. The adsorption equilibrium is in good agreement with the Langmuir Isotherm ($R^2 = 0.997$), and the kinetics analysis suggests the adsorption is a pseudo-second-order process ($R^2 = 0.992$), confirming the chemisorption of sulfate species on IOICBs. After sulfate adsorption, the IOICBs were regenerated in 0.1 M NaOH solution, reused for multiple sorption/desorption cycles, and the reusability remained at over 83% after four consecutive cycles. Thus, IOICBs are potential absorbents for removing industrial pollutants such as sulfate ions from wastewater.

1 | Introduction

During mining and metallurgical processing of sulfide minerals, for example pyrite, the oxidation of sulfide sulfur results in the generation of a high amount of sulfate in process, drainage and waste waters (reaction 1). For instance, neutral or acid mine drainage and effluent water released from the upstream and downstream metal extraction processes are significant sources of acidity and sulfates in surface and groundwater. The high concentration of sulfates in natural water streams could adversely

affect human and aquatic life [1–4]. The maximum tolerable sulfate level in industrial wastewater ranges between 250 and 500 mg/L. Typical sulfate levels in domestic sewage can vary between 20 and 500 mg/L, whereas mine and other industrial effluents may contain several thousand mg/L of sulfate species [5]. A modest amount of sulfate in water has a negligible impact on human health. Still, when the sulfate content surpasses 500 mg/L, it can lead to acute diseases such as diarrhea, dehydration, and gastrointestinal dysfunction, whereas polioencephalomalacia occurs in animals. In addition, sulfate-containing sediments in lakes, rivers, and the ocean can induce detrimental impacts on the structural integrity of metallic structures, that is, pipes, ships, offshore oil and gas drilling rigs, and bridges, due to extensive scaling and accelerated corrosion [6, 7].

$$2FeS_2 + 7O_2 + 2H_2O \rightarrow 2Fe^{2+} + 4SO_4{}^{2-} + 4H^+ \quad (1)$$

Enriched sulfate water has been treated using a variety of techniques, including membrane technologies [6], ion exchange [7], adsorption [8], and chemical and biological treatment methods [5, 9]. On a commercial scale, the selection of the treatment process is dependent on the mine water chemistry and mining operation [1]. For instance, in the case of membrane separation processes, the pre-treatment of the membrane is necessary to prevent membrane fouling. Also, membrane technologies and ion exchange processes are considered uneconomical for treating large amounts of contaminated mine water [1, 5].

Adsorption has proven to be one of the most cost-effective, biocompatible, and environmentally friendly wastewater treatment methods [10, 11]. For example, conventional adsorbents include biomass, agricultural waste, nanosized metal oxides (NMOs), activated carbon, and others. With simple chemical modification processes, the adsorption capacity of activated carbon, which is considered the most effective method to remove contaminants from water, can be significantly enhanced. However, the retrieval of powdered activated carbon from treated water can be relatively complex [12].

Iron oxide has a remarkable abundance of active sites readily available for adsorption. This abundance of active sites allows efficient capture of contaminants across a broad range of pH values, making it suitable for a wider variety of applications than other adsorbent materials [13]. Iron oxide nanomaterials efficiently remove heavy ions; however, their frequent challenges include the precipitation of iron oxide and limited reusability [14]. Polymeric-based adsorbents utilizing polysaccharide chitosan as a matrix are emerging materials in adsorption science [15]. Its outstanding adsorption properties primarily arise from the amino ($-NH_2$) and hydroxyl (–OH) groups present in chitosan within its polymer matrix [16]. One of the critical advantages of chitosan lies in its versatility of application. It can be readily adapted to various physical forms, including powders [15], nanoparticles [17], hydrogels [18], fibers [19], and beads [20]. This makes it a highly versatile material for environmental and separation processes. Recent studies have shown that chitosan grafted with polyaniline and reinforced with cobalt ferrite nanoparticles forms highly efficient nanocomposites for wastewater remediation, capable of removing a broad spectrum of heavy metals such as Pb^{2+}, Cu^{2+}, Cd^{2+}, Zn^{2+}, and Cr^{2+} with efficiencies exceeding 95%. The optimized Ch-g-PANI/CoFM-5% composite achieved rapid adsorption equilibrium within 90 min, followed by multilayer Freundlich isotherm behavior, and maintained strong regeneration capacity over multiple cycles, underscoring its potential as a sustainable treatment material [21]. Another approach involved fabricating chitosan/gelatin membranes reinforced with graphene oxide nanoplatelets grafted with natural rosin acids (GO-g-R), yielding sustainable bio-membranes with enhanced strength and photocatalytic performance. An optimized CGe-GO-g-R30% membrane had ~96.5 N/mm^2 tensile strength, strong antibacterial activity, and up to 98.4% dye removal efficiency under solar irradiation, following Langmuir isotherm and pseudo-second-order kinetics, while retaining reusability across cycles [22]. Chitosan/polyvinyl alcohol membranes incorporated with graphene oxide modified by rosin and silver nanoparticles demonstrated strong dual functionality for water treatment, simultaneously targeting heavy metals and microbial contaminants. The optimized composite (3 wt.% decorated GO) achieved removals between 85% and 99.7% for different metal ions, while also displaying notable antibacterial performance and improved tensile strength (~48 MPa), underscoring its promise for agricultural and irrigation applications [23]. Hybrid polyvinyl chloride/dapsone membranes embedded with silver nanoparticles were engineered to enhance pollutant removal from contaminated water, offering combined efficiency against heavy metals, microbial species, and nutrient compounds such as phosphates and nitrates. The optimal composition containing 0.2% Ag NPs achieved removal rates between 71% and 95% depending on ion type, while also improving porosity, tensile strength, and antibacterial properties, making it a promising multifunctional membrane for environmental and biomedical applications [24]. Recent work demonstrated that incorporating natural rhubarb extracts into polyvinyl alcohol/chitosan films yields bio-adsorbent membranes with enhanced structural and functional properties. The optimized formulation, containing 10% rhubarb extract, had superior antioxidant performance and achieved nearly complete removal (≈96%) of both cationic and anionic dyes from wastewater. These findings highlight the potential of plant-derived antioxidants to improve membrane biocompatibility, mechanical stability, and adsorption efficiency for sustainable water treatment applications [25]. This adaptability allows researchers to tailor chitosan-based adsorbents to specific applications and optimize their performance for different tasks. For instance, a granular sorbent bead based on chitosan and $FeCl_3$ was effectively developed to enhance the removal of nitrate and phosphate. The ability to sorb nitrate and phosphate experienced a substantial enhancement. Moreover, the material demonstrated excellent stability and reusability, validated through sorption–desorption cycles [26]. Chitosan offers many benefits, such as biodegradability, presence in abundance, biocompatible and non-toxic nature, its limited accessible surface area, low mechanical stability, and partly inaccessible functional groups (due to its semi-crystalline structure), which present challenges for optimal performance [27]. To address chitosan's limitations, several modification techniques have been used, employing both physical and chemical methods [28]. Compared to pristine chitosan, bead systems derived from this natural polymer have several distinct advantages. For instance, they demonstrate enhanced capacity for removing contaminants from

wastewater, offering a promising opportunity for environmental remediation [29].

Recent investigations further reinforce the versatility of chitosan-based composites in targeting both cationic and anionic pollutants. For example, Azzeddine et al. developed cross-linked and uncross-linked chitosan gel beads derived from shrimp waste, demonstrating their strong affinity for heavy metal cations and highlighting how bead morphology and crosslinking influence adsorption performance and stability. Under optimized experimental conditions, chitosan gel beads cross-linked with epichlorohydrin achieved a fluoride removal efficiency of 76%, which was notably higher than the 61% removal obtained using non-cross-linked beads [30]. Similarly, Alqarni et al. reported a crosslinked chitosan–hydroxyapatite–TiO_2 biocomposite that achieved efficient fluoride removal from drinking water, with mechanistic insights confirming the strong binding of oxyanions to the composite framework [31]. In another study, Alqarni and co-workers synthesized novel chitosan-based surfactants, which showed enhanced interactions with both positively and negatively charged species, thereby extending the applicability of chitosan derivatives for wastewater treatment. A comparative evaluation of Cr(VI) uptake by pristine chitin and the chitin@metakaolin (CHt@M.K.) composite revealed that CHt@M.K. exhibited a markedly higher adsorption capacity of 278.88 mg/g, nearly twice that of chitin, at pH 5.0 within 120 min. The adsorption behavior was best described by the Langmuir isotherm model, confirming the monolayer nature of Cr(VI) adsorption on CHt@M.K [32]. Furthermore, Algethami et al. developed a shrimp waste–derived chitosan-alumina composite that demonstrated efficient removal of hexavalent chromium (Cr(VI)), with an impressive adsorption capacity of 433.12 mg/g at pH 4.0 within 120 min. The study also highlighted the material's dual advantage of targeting anionic pollutants while maintaining good regeneration potential over successive cycles [33].

Numerous research studies have been undertaken on chitosan to enhance its adsorption properties, and a considerable number of successful outcomes have been achieved so far. For instance, Bernd et al. explored the sulfate adsorption capabilities of chitosan bead systems at a pH of 5, utilizing a range of sulfate concentrations between 50 and 1000 mg/L. Their findings revealed that beads with minimal cross-linking demonstrated a moderate sulfate uptake of 35 mg/g. Beads subjected to cross-linking and subsequent treatment with Ca^{2+} showed significantly higher sulfate adsorption, reaching a maximum capacity of 140 mg/g [34]. Janek et al. investigated the interaction of sulfate ions (SO_4^{2-}) with the polymer chains of chitosan under acidic conditions. Their study demonstrated that chitosan serves as an effective adsorbent for sulfate ions, with analysis conducted using an Inductively Coupled Plasma-Optical Emission Spectrometer (ICP-OES) [35]. Atif et al. created a composite material primarily composed of kaolinite (a plentiful mineral in Egypt), a cross-linker copper ion, and chitosan for sulfate and chloride removal from groundwater. In highly acidic conditions, the removal percentages for sulfate and chloride ions reached approximately 92%, while at a neutral pH, the removal was around 70% [36]. Billah et al. presented a mechanistic study on phosphate (an anionic species) adsorption onto a novel chitosan-based material; their findings reveal insights into adsorption sites, binding mechanisms, and pH dependency, underscoring the capability of chitosan composites for oxyanion removal under realistic conditions. This work adds to the growing evidence that chitosan-based composites can efficiently remove anions such as phosphate in addition to cations [37].

However, compared to extensive research on phosphate [38] and nitrate adsorption [39], studies on sulfate adsorption remain insufficient, aligning with recent reviews that highlight limited research on this oxyanion's (SO_4^{2-}) removal through adsorption, which points to a potential gap to be filled. Thus, this study highlights the significance of employing chitosan-coated iron oxide composite beads and improving adsorption capacity by electrostatic interactions and chemisorption, with a particular focus on sustainability. While various adsorbents in the literature show effectiveness, they have a low reported adsorption capacity, and their limitations become apparent when dealing with trace amounts. There is a demand for increased adsorption performance, especially for lower sulfate concentrations, and with convenient regeneration that offers friendly environmental solutions.

In the present study, the iron oxide-incorporated chitosan beads (IOICBs) were synthesized. Briefly, the Fe_3O_4 nanoparticles (NPs) were produced by the co-precipitation method. These NPs were embedded in chitosan using an inverted suspension cross-linking method in the presence of polyvinylpyrrolidone (PVP), which promoted the cross-linking of chitosan. These synthesized IOICBs were then employed to remove sulfate from simulated wastewater via batch adsorption. The effects of pH, initial sulfate concentration, contact time, and dosage on the sulfate removal efficiency of the IOICBs were evaluated. The adsorption isotherms and kinetic models were employed to comprehend the adsorption mechanism and characteristics of the IOICBs, and reusability was tested over four consecutive adsorption cycles.

2 | Materials and Methods

2.1 | Reagents

A high-viscosity chitosan $(C_6H_{11}NO_4)_n$ with a molecular mass of 500,000 having 84% level of deacetylation, sodium sulfate (Na_2SO_4) as a source of sulfate ions, acetic acid (CH_3COOH, glacial 99%–100%), hydrochloric acid (HCl), anhydrous sodium hydroxide pellets (NaOH, purity = 98%), and PVP were purchased from Sigma-Aldrich, Germany. For the synthesis of iron oxide, iron (III) chloride hexahydrate ($FeCl_3.6H_2O$, $M_w = 270.30$) and iron (II) chloride tetrahydrate ($FeCl_2.4H_2O$, $M_w = 198.81$) were used as received from Duskan, China. Ammonium hydroxide solution (NH_4OH, purity = 32%) was purchased from Merk, South Korea. All analytical grade chemicals obtained were used without any additional purification. MilliQ deionized (DI) water, having low conductivity (< 20 μS/cm), was used throughout this study.

2.2 | Synthesis of Fe_3O_4 Nanoparticles

Iron oxide NPs were prepared via the co-precipitation process [40]. Initially, 8 mmol of $FeCl_3.6H_2O$ and 4 mmol of $FeCl_2.4H_2O$ were added to DI water (100 mL) using a magnetic stirrer

(250 rpm) at 20°C. In this solution, 5 mL of 32% aqueous ammonium hydroxide (NH_4OH) was added to increase the pH of the solution and precipitate the iron oxide (the color turned dark brown from yellow). The supernatant liquid was initially decanted after precipitation, and the residues were washed in DI water multiple times until the pH reached 5.4 at room temperature [41]. These precipitates were centrifuged for 2 h at 200 rpm, followed by vacuum filtration and drying overnight at 60°C in a vacuum oven. The dried residues were ground to fine particles employing a pestle and mortar, as shown in Figure 1 (top panel) [42].

2.3 | Synthesis of Iron Oxide-Incorporated Chitosan Beads (IOICBs)

IOICBs were prepared using the chemical loading method described before [43]. The hybrid beads were created by pouring acetic acid (2.6% v/v) into the solution of chitosan (3.5 g) in 50 mL of polyvinylpyrrolidone (PVP) and agitating at 450 rpm for 12 h. The as-prepared iron oxide NPs (1 g) were added to this solution during continuous stirring. This suspension was sonicated for 30 min at room temperature for homogenization and deaeration, and then dropwise added to a 1 M NaOH solution to synthesize the IOICBs, which were filtered and washed several times using deionized water. These beads were dried at 60°C in a vacuum oven for 12 h. A yield of almost 4–4.2 g was achieved after some handling/washing losses. The schematic illustration for synthesizing iron oxide NPs and IOICBs is shown in Figure 1.

2.4 | Characterization

The morphology of the iron oxide NPs and IOICBs was examined using a scanning electron microscope (SEM) (JSM 6700I, JEOL, Japan) at accelerating voltages of 20 and 10 kV, respectively. The compositional analysis was performed using an Energy Dispersive Spectroscopy (EDX) detector (JEOL, Japan) attached to this microscope. The formation of Fe_3O_4 NPs was confirmed by x-ray (powder) Diffraction (XRD), and the diffraction patterns of the NPs and IOICBs were recorded with a D2 phaser, Bruker Germany, by using Cu-Kα radiation (λ = 1.54 Å) and scanning within 20°–90° of 2θ angle, having a step size rate of 0.02 s^{-1}. Fourier Transform Infrared spectroscopy (FTIR) of the Fe_3O_4 NPs and IOICBs was performed (both before and after sulfate adsorption) using the Perkin-Elmer-283B FTIR spectrometer (The USA) at 4 cm^{-1} resolution and within the range of 400–4000 cm^{-1} wavenumber. The Brunauer–Emmett–Teller (BET) method was used to determine the average pore size of the beads and specific surface area measured by N_2 adsorption at 77 K in the ASAP 2420 system (Micromeritics, The USA). The samples were degassed for 1 h at 110°C before the batch adsorption studies using the VacPrep 061 instrument (Micromeritics, The USA).

2.5 | Sulfate Removal Efficiency and Capacity

To perform adsorption studies, the simulated sulfate solutions of various concentrations (30 mL) were initially added to 50 mL laboratory glass bottles. A known amount (adsorbent dosage) of IOICBs was then added to these solutions and stirred by a mechanical shaker for various durations at 120 rpm. Each time, a control solution without IOICBs was placed with an experiment to determine the initial known concentration for comparative calculation. The experiments were performed in triplicate, and mean values are reported. After separating the IOICBs, the remnant solutions were characterized by UV–Vis spectrophotometry (Agilent 8453 Spectrophotometer, JENWAY, UK). After adsorption, the sulfate concentration in the test solutions was estimated from the UV–Vis spectra obtained within 200–800 nm wavelengths and compared with the as-prepared sulfate solution. To determine the effect of a single parameter, the conditions

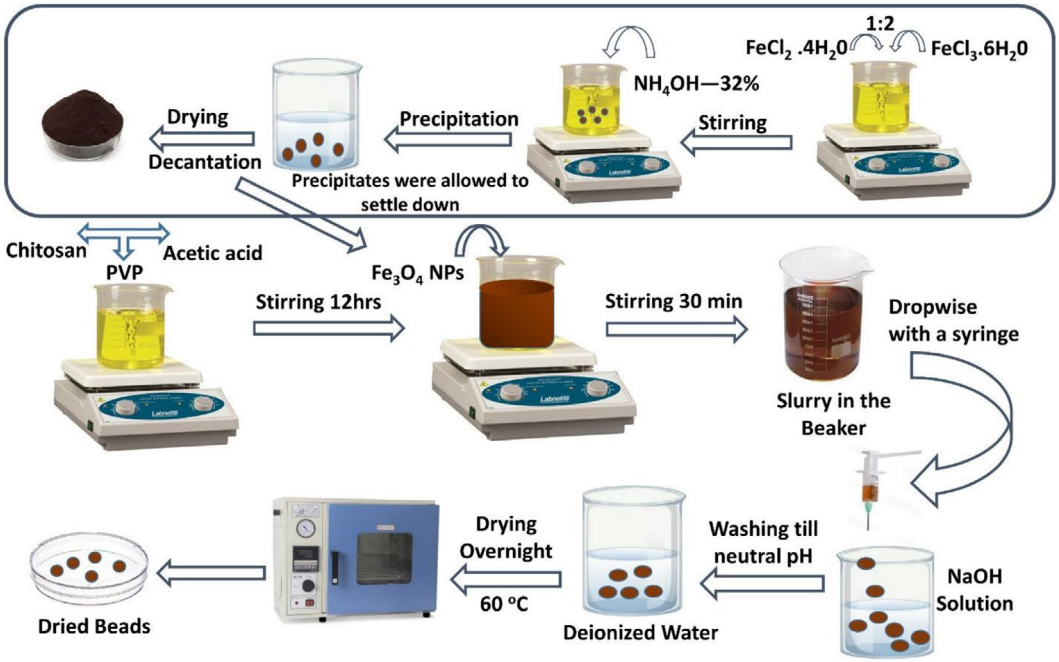

FIGURE 1 | Schematic representation of the iron oxide NPs (top panel) and the IOICBs synthesis process (bottom panel).

of pH [1–8], concentration of sulfate solution (50–300 mg/L), IOICBs dosage (20–50 mg), and contact time (6 h) were varied to determine optimum adsorption and mechanism. The adsorption capacity and removal efficiency of the IOICBs for sulfate were calculated using the following formulas (Equations 1 and 2, respectively) [44, 45].

$$q\left(\frac{mg}{g}\right) = \frac{(C_o - C_e)}{m} \times V \tag{1}$$

$$\eta = \frac{(C_o - C_e)}{C_o} \tag{2}$$

where C_0 and C_e are the sulfate concentrations in (mg/L) before and after adsorption, respectively. 'V' is the sample volume (L) taken for the analysis, while 'm' is the mass (g) of the adsorbents used during testing.

2.6 | Adsorption Isothermal Models

The adsorption mechanism was evaluated by applying the Langmuir and the Freundlich isotherms [46]. The relative changes in the adsorption and desorption behavior depend on the surface coverage, which was explained by the Langmuir isotherm. Adsorption is proportional to the concentration of the freely available active sites on the surface of the IOICBs (homogeneous surface). In contrast, desorption is proportional to the extent of the surface coverage or, in other words, the amount of surface active sites occupied by the adsorbate is dictated by the Langmuir isotherm as given in Equation (3) [47].

$$\frac{C_e}{q_e} = \frac{1}{q_m K_L} + \frac{C_e}{q_m} \tag{3}$$

Here, C_e (mg/L) is the concentration of adsorbate at equilibrium, q_e (mg/g) is the amount of adsorbate on the surface of the adsorbent material, whereas q_m (mg/g) is the maximum adsorption capacity of the adsorbent. K_L (mg/g) is the Langmuir constant associated with the variation in the amount of porosity and active surface area of the adsorbent. This suggests that an adsorbent material with a larger surface area and porous structure would increase the adsorption capacity.

$$R_L = \frac{1}{1 + K_L C_o} \tag{4}$$

where C_0 (mg/L) is the initial concentration of adsorbate, K_L (mg/g) is the Langmuir constant. R_L provides information about the nature and shape of the adsorption isotherm to be either favorable ($0 < R_L < 1$), unfavorable ($R_L > 1$), linear ($R_L = 1$), or irreversible ($R_L = 0$) as per Equation (4).

Adsorption on heterogeneous surfaces is subjected to the Freundlich isotherm, which describes the adsorbent surface's heterogeneity, the active sites' distribution, and surface energies as defined in Equation (5) [48].

$$logq_e = logK_F + \frac{1}{n} logC_e \tag{5}$$

where q_e (mg/g) is the amount of the adsorbed species at equilibrium, C_e (mg/L) is the concentration of adsorbate at equilibrium, K_F (L/mg) is the adsorption capacity, and *1/n* is the adsorption intensity. These factors indicate that both the relative distribution of energy and the heterogeneity of the adsorbent sites are evaluated from the slope and intercept of the linear plot of log q_e versus log C_e, respectively.

2.7 | Adsorption Kinetic Models

The pseudo-first-order and pseudo-second-order models were tested to investigate the kinetics of sulfate adsorption on the IOICBs [49, 50]. Using Equations (6) and (7), the adsorption parameters are calculated as follows:

$$\ln(q_e - q_t) = lnq_e - K_1 t \tag{6}$$

$$\frac{t}{q_t} = \frac{1}{K_2 q_e^2} + \frac{t}{q_e} \tag{7}$$

where q_t (mg/g) is the amount of adsorbate adsorbed at a given time 't', q_e (mg/g) is the amount of adsorbate adsorbed at equilibrium, k_1 (1/min) and k_2 (g/(mg.min)) are the rate constant of the pseudo-first and second-order models, respectively [51].

2.8 | Reusability Test

A set of experiments was conducted to investigate the regeneration of IOICBs after each adsorption cycle. The regeneration was carried out by first mixing 90 mL of a 250 mg/L sulfate-containing solution (pH = 2) at room temperature for 4 h under continuous stirring. After each adsorption cycle, the IOICBs were washed with DI water three times and treated with 250 mL of 1 M NaOH under constant stirring at 120 rpm for 12 h. This allowed the elution of chemically bonded sulfate ions from the IOICBs during desorption. As NaOH was used in low quantities, it posed no environmental hazards. Thus, the IOICBs were washed with plenty of DI water until the pH of the wash water reached the pH of DI water, followed by drying at 60°C for 4 h. The IOICBs were then kept in a desiccator until further use.

3 | Results and Discussion

3.1 | Morphological and Structural Characterization of the IOICBs

The morphology of the as-synthesized iron oxide NPs is shown in Figure 2a,b. The NPs measured from SEM images are found to be of various sizes (36–53 nm) and have irregular shapes with porous structures. This is also evident from the BET analysis with a mean NP size = 35.7 nm, total area of pores = 68.723 m^2/g, total pore volume = 0.03 cm^3/g, and specific surface area equaled 167.8606 ± 0.9052 m^2/g. In addition, the fine-size iron oxide NPs were found to be agglomerated due to possible steric effects of surface active sites and inter-particulate interaction [52, 53]. On the other hand, the formation of spherical-shaped (elliptic) micro IOICBs is evident in Figure 2c. The surface morphology of these IOICBs was found to be uneven due to the formation of

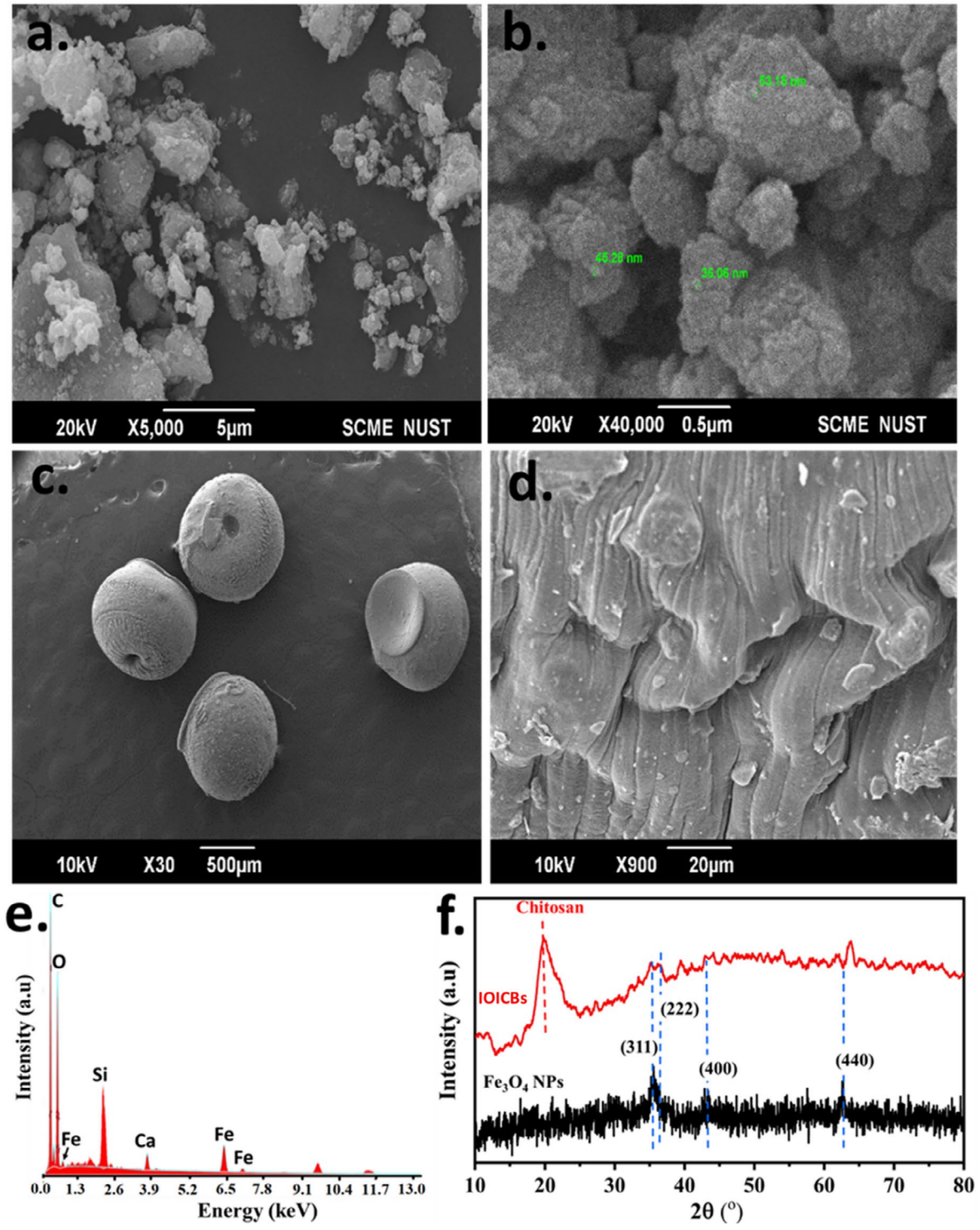

FIGURE 2 | SEM images of Fe_3O_4 NPs (a) low and (b) high magnification, (c) and (d) as-synthesized IOICBs microbeads, (e) EDX spectrum of IOICBs, and (f) XRD patterns of the synthesized iron oxide and IOICBs.

macro-porous channels within the top chitosan layer. A unidirectional flow pattern was observed on the wall of these macropores, which was possibly attributed to the cross-linking groups of chitosan (amine and –OH) in the vigorous stirring action of chitosan/PVP/iron oxide NPs, which was facilitated by PVP in the formation of IOICBs, as shown in Figure 2d. Owing to the formation of the rough and macro-porous surface of the IOICBs, the presence of large amounts of surface active sites can be expected to facilitate sulfate adsorption and be beneficial for better ionic adsorption [54]. This is confirmed by the BET total area of pores ($0.096\,m^2/g$) with a total pore volume of $9 \times 10^{-5}\,cm^3/g$ and a mean pore width of 1.756 nm. Furthermore, the BET results of IOICBs ($0.3255 \pm 0.0138\,m^2/g$) firmly agree with the SEM findings. Additionally, the EDX results show that sulfur is absent in the IOICBs before sulfate adsorption studies in Figure 2e.

The XRD patterns of both iron oxide and IOICBs are shown in Figure 2f. The XRD pattern of the as-synthesized iron oxide NPs

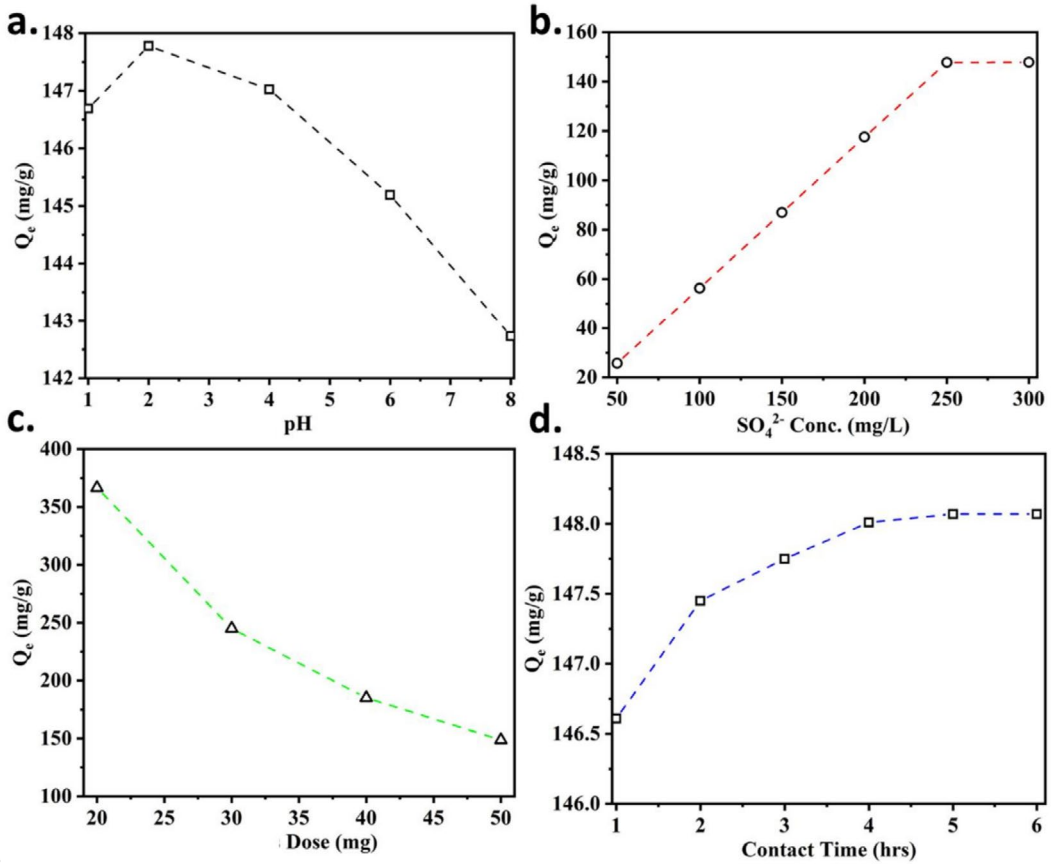

FIGURE 3 | Effect of (a) pH, (b) initial sulfate concentration, (c) IOICB dose, and (d) IOICB contact time on the adsorption capacity of IOICBs for sulfate species at room temperature.

suggested the presence of magnetite (Fe_3O_4) as the major phase, following the JCPDS 00-001-1111 reference pattern [55]. For instance, the diffraction peaks at 2θ of 35.45°, 37.12°, 43.03°, and 62.72° correspond to the diffraction from the (311), (222), (400), and (440) crystallographic planes of magnetite, respectively [56]. The origin of broader diffraction peaks was attributed to the formation of a fine particle size of the Fe_3O_4.

The XRD pattern of the IOICBs had the characteristic diffraction peaks of pure chitosan at 2θ = 12.17° and 20.16°, which correspond to crystallinity in the polymeric chains of the chitosan [57]. These low-intensity broad diffraction peaks were found to be broad and lower in intensity compared to the intensities for pure chitosan. This is due to a loss in the crystallinity of chitosan as it forms an amorphous material with Fe_3O_4 NPs. The magnetic nature of these beads is clear through the prominent diffraction peaks of magnetite NPs at 2θ = 35° and 62°, more prominently, while other relevant peaks of NPs are also present at 2θ = 43°, 53.54°, and 57.16°. The repression of these peaks is seen because of the embedding of magnetite NPs into chitosan beads [58].

3.2 | Effect of Operating Parameters

The adsorption of sulfate species on IOICBs depends on operating parameters such as solution pH, initial sulfate concentration, IOICB dose, and overall residence (contact) time of the IOICBs in the sulfate-containing solution. Therefore, to determine the optimized parameters, the maximum adsorption capacity of the as-synthesized IOICBs was determined under various applied conditions, and the results are discussed in the following sections. The experimental data set Table S1, the descriptive statistical analysis (Table S2), the Normal distribution curve of adsorption capacity of sulfate removal (Figure S1), and the Pearson correlation heatmap (Figure S2) demonstrating the interaction behavior between input experimental parameters and adsorption capacity (output) are presented in the Data S1.

3.2.1 | Effect of pH

The effect of pH on the adsorption capacity of IOICBs was determined in 250 mg/L sulfate solutions. The pH of the solutions was controlled to between 1 and 8 with the addition of either HCl or NaOH in the sulfate-containing solutions. The experiments were conducted by adding 50 mg of IOICBs to 30 mL of sulfate-containing solutions under vigorous mechanical shaking for 4 h at room temperature (23°C ± 1°C). As shown in Figure 3a, pH significantly influenced the sulfate removal capacity of the IOICBs. Regarding sulfate removal capacity (Q_e), the IOICBs performed better in acidic media than in alkaline conditions. For instance, a maximum sulfate adsorption capacity of 147.6 mg/g was obtained at pH 2.0; a similar trend was reported in the literature [8]. The strong electrostatic attraction between the positively charged active sites on the IOICBs and the sulfate anions

is believed to be the primary cause of their high adsorption at low pH. The highly acidic environment causes the protonation of the $-NH_2$ functional groups of the chitosan, resulting in the increased electrostatic interaction of the adsorbate anions (i.e., HSO_4^- and SO_4^{2-}) [59]. On the other hand, as stated above, the acidic pH was controlled by adding dilute HCl, and the influence of Cl^- ions on the specific sulfate adsorption was not evaluated. Increased solution pH resulted in decreased sulfate ion adsorption due to the poor protonation of the IOICBs. At pH 8, the specific adsorption of OH^- ions could compete with sulfate ions and limit the adsorption capacity of the IOICBs, as evident from the low Q_e value of 142.6 mg/g (Figure 3a). In other words, it is suggested that the partial adsorption of OH^- ions could decrease the sulfate adsorption capacity on the IOICBs surface [60, 61].

3.2.2 | Effect of Initial Sulfate Concentration

The maximum adsorption capacity of the IOICBs as a function of sulfate concentration in water at a pre-optimized pH value of 2 was measured under the same conditions as described above (Section 3.2.1). Figure 3b shows the effect of initial sulfate concentration (varied from 50 to 300 mg/L) on the Q_e of the IOICBs at room temperature. A direct relationship between Q_e and initial sulfate concentration was observed from the linear trend up to 250 mg/L initial sulfate concentration. A maximum Q_e of 147 mg/g was measured at this concentration and became constant at sulfate concentration ≥ 250 mg/L, indicating saturation. This highest Q_e demonstrated the maximum sulfate adsorption capacity of the IOICBs. This indicated that after interacting with sulfate ions, the surface active sites within the porous structure of IOICBs become fully saturated with sulfate species and represent the maximum surface coverage achievable under applied conditions. The maximum adsorption of the sulfate ions is only possible if these species can readily approach the surface pores of the IOICBs; thus, vigorous mechanical shaking applied during this process is considered necessary. In addition to mechanical shaking, an increase in initial sulfate concentration also facilitates the effective mass transport of the sulfate species towards the active sites on the IOICBs [61, 62].

3.2.3 | Effect of IOICB Dose

The amount of IOICBs used in the adsorption analysis is critical in defining the effluent concentration and significantly influences the process economics. Various IOICB dosages (from 20 to 50 mg) were tested in 30 mL of solution containing 250 mg/L of sulfate, at pH 2.0 and a residence time of 4 h, under continuous stirring conditions at room temperature. A decline in Q_e was observed with an increase in IOICB concentration, attributed to the saturation of the surface active sites and the limiting amount of sulfate ions left in the solution with an excess of IOICB dosage. Notably, the amount of sulfate adsorbed (in mg) by the IOICBs can be calculated by multiplying Q_e by the dosage in grams. The maximum adsorption was achieved at 0.02 g of IOICB dosage, as shown in Figure 3c. These results indicate that compared to the 0.05 g of IOICB dosage, the amount of sulfate removed from the solution was slightly higher at 0.02 and 0.03 g of IOICB dosage. Based on these results, approximately 1.67 g of IOICBs per liter (equal to 50 mg in 30 mL in this study) of the solution was considered the optimal concentration to achieve maximum sulfate adsorption for further tests [61, 63].

3.2.4 | Effect of Contact Time

The effect of IOICB contact time with the sulfate-containing solution is also an important parameter to optimize process conditions. Figure 3d shows the slight increase in Q_e with contact time, which becomes constant beyond 4 h. In other words, the adsorption capacity of the IOICBs achieved a saturation limit in 4 h of interaction with the sulfate solution. It is believed that specific adsorption of sulfate ions on IOICBs proceeds in two phases: rapid initial adsorption of the sulfate ions in the first 2 h, followed by a time-dependent adsorption to reach the maximum (saturation limit) after 4 h [64].

3.3 | Adsorption Isotherms

The adsorption isotherms were obtained under the optimized conditions described above, that is, 50 mg (1.67 g/L) IOICBs dosage was added in sulfate-containing solutions at pH 2 under continuous stirring on a mechanical shaker for 4 h at room temperature (23°C). As per Langmuir and Freundlich's isotherms, the adsorption capacity was plotted versus equilibrium sulfate concentration, as shown in Figure 4. A comparison between these isotherms and the experimental data was made, and the validity of these models was assessed based on linear fitting (R^2 values), as given in Table 1. The Langmuir isotherm exhibits monolayer adsorption of the sulfate, suggesting homogeneously organized identical active sites on the surface of the adsorbent material. On the other hand, the Freundlich model is governed by the adsorption of species in multilayers and represents the interaction between the adsorbed molecules in addition to surface coverage at the active site. In other words, the Freundlich isotherm also implies that adsorption is independent of the number of available active sites on the adsorbent surface. The adsorption equilibrium data were found to fit well with both the Langmuir and Freundlich isotherm models, indicating that the adsorption process involves a combination of monolayer and heterogeneous surface adsorption mechanisms.

3.4 | Adsorption Kinetics

Figure 5 shows a comparison between experimental data with the pseudo-first (Equation 6) and pseudo-second-order (Equation 7) kinetic models for the adsorption process. The experimental data had a good linear fit to the pseudo-second-order adsorption model ($R^2 = 0.992$). In contrast, the regression coefficient ($R^2 = 0.694$) is a total misfit with the experimental data for the pseudo-first-order kinetic model. The equilibrium adsorption capacity from experimental data (148.07 mg/g) is close to the predicted value of 159.74 mg/g using pseudo-second order, compared to the value of 0.823 mg/g obtained from pseudo-first-order, as shown in Table 2. Also, the 2nd order adsorption rate constant of 2.2×10^{-3} (g/(mg·min)) is suitable and justified by the interaction mechanism. Therefore, based on these results, it is suggested that the chemisorption process governs sulfate adsorption on IOICBs.

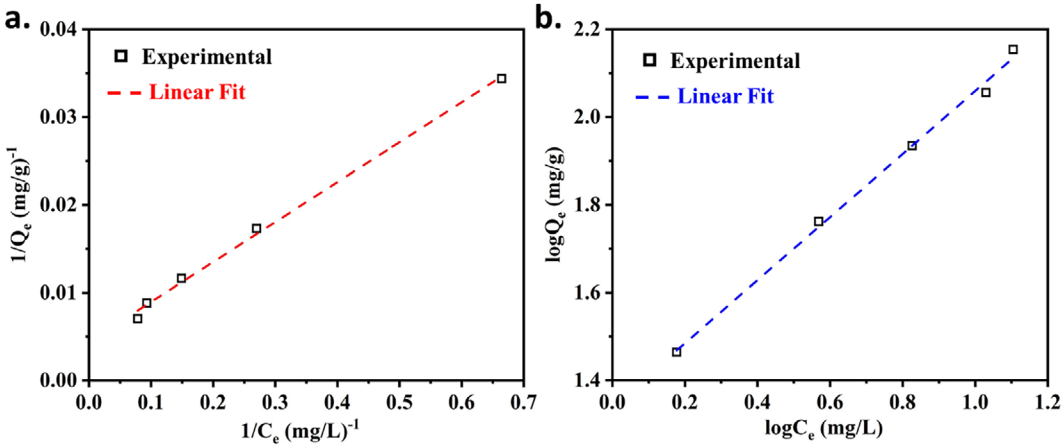

FIGURE 4 | Representation of the adsorption isotherms model fitting (a) Langmuir and (b) the Freundlich isotherms.

TABLE 1 | The obtained parameters for sulfate adsorption on IOICBs at room temperature (23°C) after Langmuir and the Freundlich isotherm model fitting.

Langmuir model					Freundlich model				
Q_{max} (mg/g)	K_L (mg/g)	R^2	AIC	BIC	N	K_F (L/mg)	R^2	AIC	BIC
226.75	498.87	0.997	−56.59	−57.37	1.391	3.822	0.9960	−23.57	−24.35

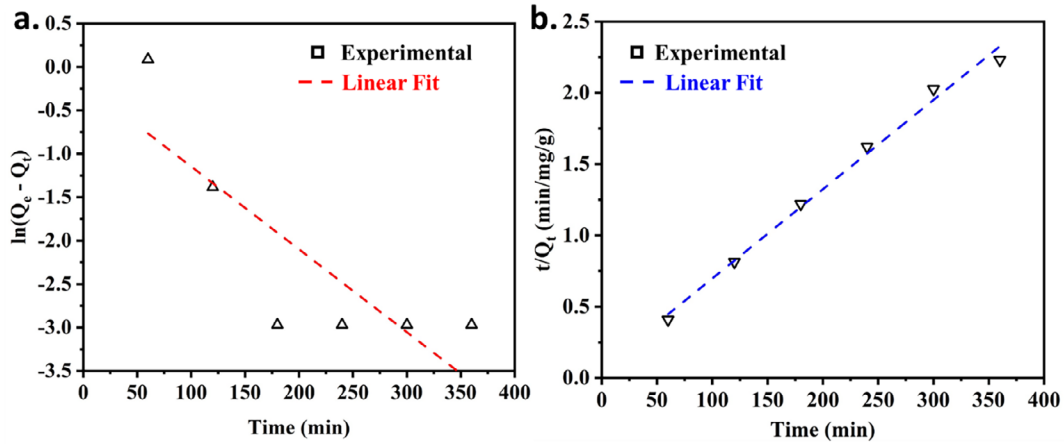

FIGURE 5 | Kinetics of sulfate adsorption on IOICBs as predicted from the (a) Pseudo 1st order and (b) Pseudo 2nd order kinetic models.

TABLE 2 | Sulfate adsorption–kinetic parameters obtained from fitting experimental data with the pseudo 1st- and 2nd-order kinetic models.

Pseudo 1st order					Pseudo 2nd order				
Q_e (mg/g)	K_1 (1/min)	R^2	AIC	BIC	Q_e (mg/g)	K_2 (g/(mg.min))	R^2	AIC	BIC
0.823	-2.64×10^{-5}	0.694	15.83	15.42	159.74	2.22×10^{-3}	0.992	−13.55	−13.96

3.5 | Regeneration Studies and Mechanism

The IOICBs were repeatedly used with fresh solution for four adsorption/regeneration cycles to evaluate their cyclic stability and adsorption capacity. As shown in Figure 6, the adsorption efficiency of the IOICBs gradually decreased over four adsorption/regeneration cycles. For instance, 98% adsorption was obtained for fresh IOICBs, which declined to approximately 83% after 4 cycles. During adsorption and regeneration cycles, the degradation of the surface functionality compromised the adsorption capacity and sulfate removal efficiency of the IOICBs. This behavior could be explained by understanding the adsorption mechanism, as shown in Figure 7. Briefly, during the adsorption process, the presence of acidic NH_4^+ functional groups on the surface of chitosan facilitates the chemisorption of the sulfate ions. These adsorbed sulfate ions can be removed from

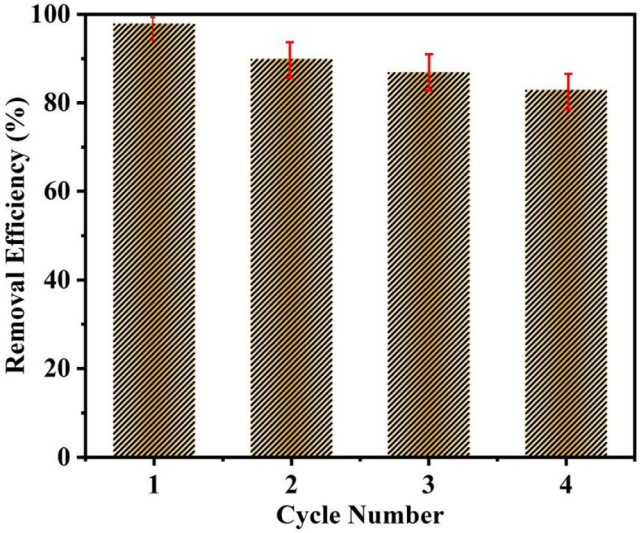

FIGURE 6 | Effect of cyclic adsorption/regeneration of IOICBs on the sulfate removal efficiency.

the surface by treating the IOICBs in NaOH solution. Owing to the competing adsorption of the OH– and removal of SO_4^{2-}, regeneration of the IOICBs was possible. Under acidic conditions, the protonation of the surface functional groups would increase the concentration of NH_4^+ species, resulting in the regeneration of the IOICBs for reuse. However, it is suggested that during the regeneration process, the OH^- species remained partially adsorbed on the active sites and reduced the adsorption capacity of the IOICBs for SO_4^{2-} species [65]. Thus, the process of sulfate adsorption on IOICBs was highly pH-dependent. A study of magnetic chitosan-Fe (III) hydrogels was reported to have a positive charge below pH 7 [66]. Another study reported the zero-point charge of Fe_3O_4-chitosan beads to be 6.94, which indicates that at pH below this value, the adsorbent remains positively charged for enhanced adsorption removal, while at pH > 6.94, this adsorbent becomes negatively charged [43]. In acidic media, the protonation of the $–NH_2$ species significantly improved the electrostatic interaction of SO_4^{2-} species. Instead, an increase in pH led to the preferential adsorption of –OH species on the IOICB's surface in comparison to the sulfate species. Furthermore, the

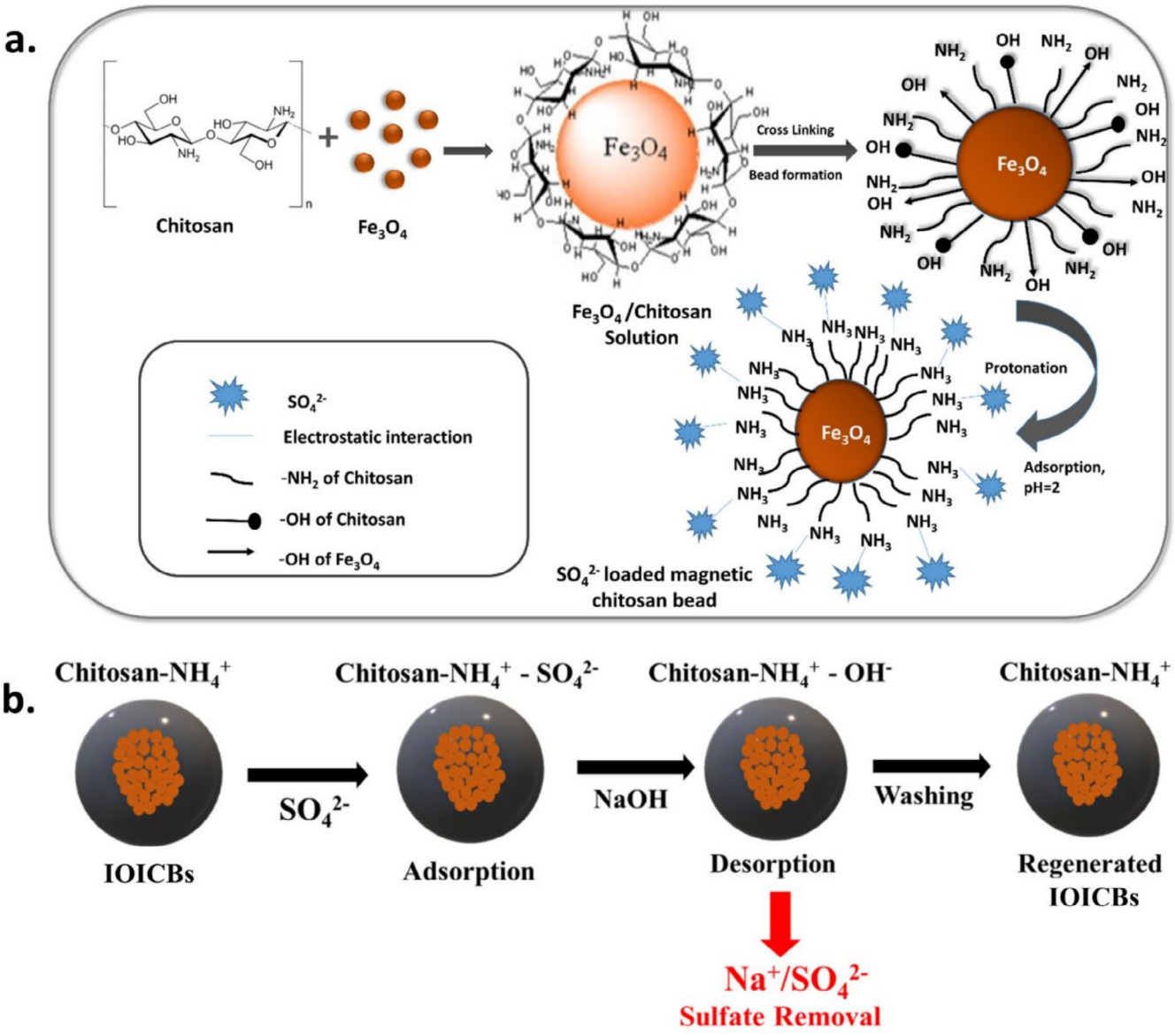

FIGURE 7 | (a) Removal mechanism (top squared panel) and (b) Regeneration for sulfate adsorption/desorption (bottom panel) on IOICBs.

partial amount of SO_4^{2-} species could irreversibly adsorb on the surface of IOICBs, decreasing their loading capacity, as discussed below.

3.6 | Post Characterization of IOICBs After Cyclic Regeneration

In comparison, the structural characterization of the as-synthesized and regenerated IOICBs was also done using FTIR spectroscopy. As shown in Figure 8a, the presence of C–H, NH_2, and –OH functional groups was evident. For instance, the absorption bands observed at 3427 and 1633 cm^{-1} were linked to the vibrations of –OH and –NH bands [67]. The peaks originating at 480 and 593 cm^{-1} are attributed to the Fe–O bond vibrations, highlighting the presence of Fe_3O_4 in the IOICBs. The stretching vibrations of C–O bonds were observed at 1109 cm^{-1}. On the surface of as-synthesized IOICBs, the bands observed at 2922 and 2853 cm^{-1} correspond to the vibrational stretching of the C–H bonds in methyl ($-CH_3$) and alkyl ($-CH_2$) groups, respectively [68]. In the case of regenerated IOICBs, the appearance of a broad peak at 3429 cm^{-1} and a more intense peak at 1631 cm^{-1} validates the presence of –OH, –NH stretching vibrations [69]. On the other hand, the peaks at 1122 and 617 cm^{-1} are associated with the vibrations of S–O and S–O–S bonds in the sulfate species that remained chemisorbed on the surface of IOICBs during the adsorption/regeneration process [70–72]. The presence of sulfur species on the surface of IOICBs was confirmed through EDX analysis, indicating specific adsorption of SO_4^{2-} as depicted in Figure 8b compared to no intensity of sulfur in pristine IOICBs (Figure 2e). The presence of these species on the regenerated IOICBs could be associated with the irreversible sulfate adsorption of SO_4^{2-}, which resulted in a decrease in adsorption capacity, as evident in the successive regeneration cycles (Figure 6). The physical appearance of the IOICBs remained unchanged after the adsorption process, demonstrating their structural integrity and stability throughout the adsorption/regeneration process. In terms of loss in adsorption capacity, no significant physical change in the morphology was observed. Based on this behavior, the decrease in adsorption capacity is likely due to the permanent occupation of SO_4^{2-} species on the active sites during the cyclic adsorption/regeneration process. Based on the information provided, the developed IOICBs show superior performance compared to other adsorbents, namely cross-linked chitosan beads and activated carbon, in terms of sulfate removal. Specifically, at low doses, the as-synthesized IOICBs have the highest adsorption capacity (147.7 mg/g) under highly acidic conditions, as shown in Table 3. The high

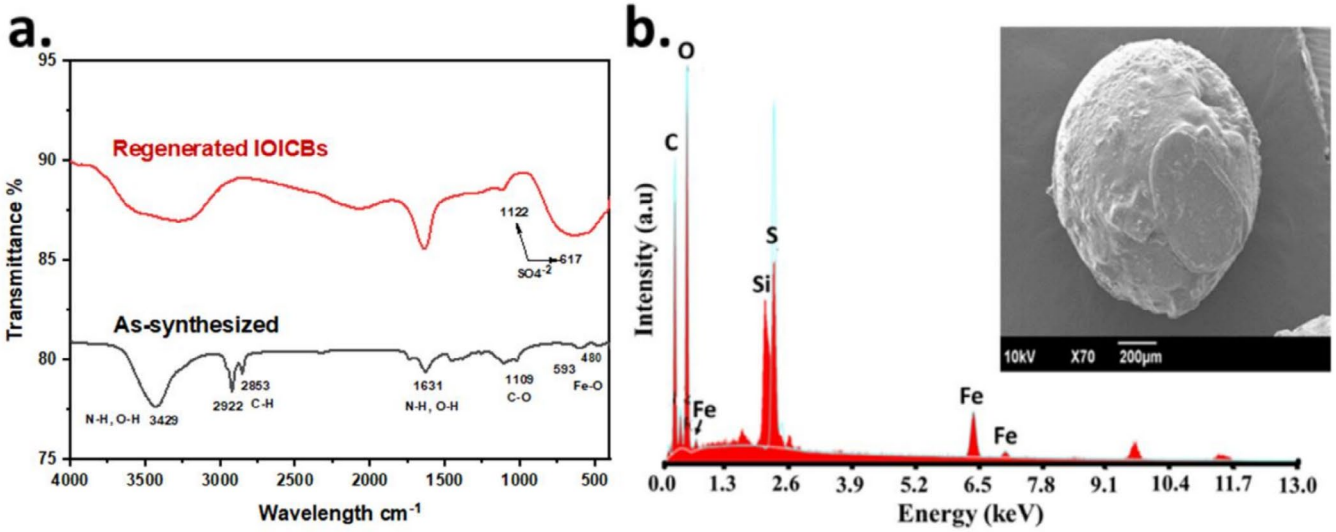

FIGURE 8 | Characterization of the IOICBs after cyclic adsorption/regeneration process (a) FTIR spectra, (b) EDX analysis, and morphology of the retrieved IOICB.

TABLE 3 | Comparing the sulfate adsorption capacity of IOICBs with other adsorbent materials reported in the literature.

Adsorbent	Adsorption capacity (mg/g)	pH	Concentration C_0 (ppm)	Reference (s)
IOICBs	147.7	2	250	This study
Hardwood-based AC modified with polypyrrole	45	7–7.2	250	[73]
Cross-linked chitosan beads	35	5	1000	[8, 34]
Cross-linked chitosan beads	140	5	1000	[34]
Modified Rice straw	75	6.4	500	[8]
Poly(m-phenylenediamine)	109	< 3	500	[74]

performance is indicated by the porous structural morphology on the surface of chitosan beads, which is evident from SEM results. This suggests that the IOICBs could be a more effective and efficient choice for sulfate removal under these specific conditions. However, further information is needed to fully evaluate the comparative performance of the different adsorbents, including factors such as cost, ease of synthesis, and other relevant parameters.

4 | Conclusion

Iron oxide (Fe_3O_4) NPs were produced using the co-precipitation method and were used to successfully synthesize surface-functionalized chitosan beads (IOICBs). Based on SEM, XRD, and FTIR analyses, the cross-linking –OH and $–NH_2$ groups of the chitosan shell with cubical-shaped porous Fe_3O_4 NPs in the core were found to be effective adsorbents for the removal of sulfate from water. The total pore volume and surface area of IOICBs were further supported by BET analysis. The effects of various parameters (i.e., pH of the solution, initial sulfate ion concentration, IOICB dose, and contact time) on the adsorption behavior of IOICBs were studied in batch mode. Effective sulfate removal (147.7 mg/g) was obtained at pH 2, a sulfate concentration of 250 mg/L, and room temperature (23°C) with a contact time of 4 h. The experimental adsorption data conformed to both the Langmuir ($R^2 = 0.997$) and Freundlich isotherms ($R^2 = 0.992$) along with the pseudo-second-order model ($R^2 = 0.992$). This indicates that the adsorption process involves mixed monolayer and heterogeneous surface adsorption governed primarily by chemisorption on a complex adsorbent surface. The synthesized IOICBs were successfully reused in 4 cycles and regenerated with an overall ~17% decay in adsorption capacity. Overall, under acidic conditions, the synthesized IOICBs presented good adsorption capacity and effective sulfate removal efficiency during four successive loading/regeneration cycles, owing to the protonation of the $–NH_2$ species, which significantly improved the electrostatic interaction of SO_4^{-2} species. Furthermore, the easy magnetic separation of the IOICBs from solution and their fast kinetics make them promising materials for sulfate removal from mine water.

Acknowledgments

The authors express their gratitude to the National University of Sciences and Technology (NUST) Research Directorate and the Higher Education Commission (HEC) of Pakistan for providing the necessary technical assistance and financial support per NRPU Project No. 6020. The author (M.Y.) gratefully acknowledges the support from the European Just Transition Fund within the Operational Programme: Just Transition under the aegis of the Ministry of the Environment of the Czech Republic, project CirkArena number CZ.10.03.01/00/22_003/0000045 and the Ministry of Education, Youth and Sports of the Czech Republic, Operational Programme Johannes Amos Comenius OP JAC "Application potential development in the field of polymer materials in the context of circular economy compliance (POCEK)", number CZ.02.01.01/00/23_021/0009004. The authors are further grateful for co-funding from the development process of the Centre of Polymer Systems, Tomas Bata University in Zlin, program DKRVO (RP/CPS/2024-28/002) supported by the Ministry of Education, Youth and Sports of the Czech Republic. M.Y. also expresses his gratitude for support within the "Creativity, Intelligence & Talent for the Zlin Region" (CIT—ZK) program. Open access publishing facilitated by Univerzita Tomase Bati ve Zline, as part of the Wiley - CzechELib agreement.

Conflicts of Interest

The authors declare no conflicts of interest.

Data Availability Statement

The study includes all the data that support the findings and conclusions, which can be found within the article and supplementary data file.

References

1. W. A. M. Fernando, I. M. S. K. Ilankoon, T. H. Syed, and M. Yellishetty, "Challenges and Opportunities in the Removal of Sulphate Ions in Contaminated Mine Water: A Review," *Minerals Engineering* 117 (2018): 74–90, https://doi.org/10.1016/j.mineng.2017.12.004.

2. G. Liao, D. Liao, and Q. Li, "Heavy Metals Contamination Characteristics in Soil of Different Mining Activity Zones," *Transactions of Nonferrous Metals Society of China* 18, no. 1 (2008): 207–211, https://doi.org/10.1016/S1003-6326(08)60037-0.

3. K. M. Wantzen and J. H. Mol, "Soil Erosion From Agriculture and Mining: A Threat to Tropical Stream Ecosystems," *Agriculture* 3, no. 4 (2013): 660–683, https://doi.org/10.3390/agriculture3040660.

4. G. Chen, Y. Ye, N. Yao, N. Hu, J. Zhang, and Y. Huang, "A Critical Review of Prevention, Treatment, Reuse, and Resource Recovery From Acid Mine Drainage," *Journal of Cleaner Production* 329 (2021): 129666, https://doi.org/10.1016/j.jclepro.2021.129666.

5. R. Bowell, "A Review of Sulfate Removal Options for Mine Waters," in *Mine Water 2004 – Proceedings International Mine Water Association Symposium 2*, eds A. P. Jarvis, B. A. Dudgeon, and P. L. Younger (Newcastle upon Tyne (University of Newcastle), 2004), 75–91.

6. A. Barr, "Sulphate Removal by Nanofiltration," *Filtration & Separation* 38, no. 6 (2001): 18–20, https://doi.org/10.1016/S0015-1882(01)80376-1.

7. Y. Öztürk and Z. Ekmekçi, "Removal of Sulfate Ions From Process Water by Ion Exchange Resins," *Minerals Engineering* 159 (2020): 106613, https://doi.org/10.1016/j.mineng.2020.106613.

8. W. Cao, Z. Dang, X. Q. Zhou, et al., "Removal of Sulphate From Aqueous Solution Using Modified Rice Straw: Preparation, Characterization and Adsorption Performance," *Carbohydrate Polymers* 85, no. 3 (2011): 571–577, https://doi.org/10.1016/j.carbpol.2011.03.016.

9. P. Kinnunen, H. Kyllönen, T. Kaartinen, J. Mäkinen, J. Heikkinen, and V. Miettinen, "Sulphate Removal From Mine Water With Chemical, Biological and Membrane Technologies," *Water Science and Technology* 2017 (2018): wst2018102, https://doi.org/10.2166/wst.2018.102.

10. A. Dąbrowski, "Adsorption — From Theory to Practice," *Advances in Colloid and Interface Science* 93, no. 1 (2001): 135–224, https://doi.org/10.1016/S0001-8686(00)00082-8.

11. G. Huang, C. Yang, K. Zhang, and J. Shi, "Adsorptive Removal of Copper Ions From Aqueous Solution Using Cross-Linked Magnetic Chitosan Beads," *Chinese Journal of Chemical Engineering* 17, no. 6 (2009): 960–966, https://doi.org/10.1016/S1004-9541(08)60303-1.

12. H. B. Quesada, T. P. de Araújo, D. T. Vareschini, M. A. S. D. de Barros, R. G. Gomes, and R. Bergamasco, "Chitosan, Alginate and Other Macromolecules as Activated Carbon Immobilizing Agents: A Review on Composite Adsorbents for the Removal of Water Contaminants," *International Journal of Biological Macromolecules* 164 (2020): 2535–2549, https://doi.org/10.1016/j.ijbiomac.2020.08.118.

13. P. M. B. Chagas, A. A. Caetano, M. A. Rossi, et al., "Chitosan-iron Oxide Hybrid Composite: Mechanism of Hexavalent Chromium

Removal by Central Composite Design and Theoretical Calculations," *Environmental Science and Pollution Research* 26, no. 16 (2019): 15973–15988, https://doi.org/10.1007/s11356-019-04545-z.

14. M. Li, Y. Kang, H. Ma, J. Dong, Y. Wang, and S. Kuang, "Efficient Removal of Heavy Metals From Aqueous Solutions Using Mn-Doped FeOOH: Performance and Mechanisms," *Environmental Research* 231 (2023): 116161, https://doi.org/10.1016/j.envres.2023.116161.

15. U. Upadhyay, I. Sreedhar, S. A. Singh, C. M. Patel, and K. L. Anitha, "Recent Advances in Heavy Metal Removal by Chitosan Based Adsorbents," *Carbohydrate Polymers* 251 (2021): 117000, https://doi.org/10.1016/j.carbpol.2020.117000.

16. R. S. Vieira, E. Meneghetti, P. Baroni, et al., "Chromium Removal on Chitosan-Based Sorbents – An EXAFS/XANES Investigation of Mechanism," *Materials Chemistry and Physics* 146, no. 3 (2014): 412–417, https://doi.org/10.1016/j.matchemphys.2014.03.046.

17. R. P. Medina, E. T. Nadres, F. C. Ballesteros, and D. F. Rodrigues, "Incorporation of Graphene Oxide Into a Chitosan–Poly(Acrylic Acid) Porous Polymer Nanocomposite for Enhanced Lead Adsorption," *Environmental Science. Nano* 3, no. 3 (2016): 638–646, https://doi.org/10.1039/C6EN00021E.

18. Y. Zhang, S. Lin, J. Qiao, et al., "Malic Acid-Enhanced Chitosan Hydrogel Beads (mCHBs) for the Removal of Cr(VI) and cu(II) From Aqueous Solution," *Chemical Engineering Journal* 353 (2018): 225–236, https://doi.org/10.1016/j.cej.2018.06.143.

19. M. I. Shariful, S. B. Sharif, J. J. L. Lee, U. Habiba, B. C. Ang, and M. A. Amalina, "Adsorption of Divalent Heavy Metal Ion by Mesoporous-High Surface Area Chitosan/Poly (Ethylene Oxide) Nanofibrous Membrane," *Carbohydrate Polymers* 157 (2017): 57–64, https://doi.org/10.1016/j.carbpol.2016.09.063.

20. P. Ngamsurach, N. Namwongsa, and P. Praipipat, "Synthesis of Powdered and Beaded Chitosan Materials Modified With ZnO for Removing Lead (II) Ions," *Scientific Reports* 12 (2022): 12, https://doi.org/10.1038/s41598-022-22182-4.

21. D. E. Abulyazied, H. Isawi, E. S. Ali, et al., "Fabrication and Characterization of Magnetic Cobalt Ferrite Intercalated Chitosan Grafted Polyaniline Ternary Nanocomposites for Removing Some Heavy Metals Simultaneously," *Journal of Molecular Liquids* 393 (2024): 123527, https://doi.org/10.1016/j.molliq.2023.123527.

22. H. Moustafa, E. M. Ahmed, M. Hemida, M. Rabee, and H. Isawi, "Surface Grafting GO Nanoplatelets With Antimicrobial Rosin Acids for Strengthening Photocatalytic of Chitosan/Gelatin Nanocomposites," *Diamond and Related Materials* 157 (2025): 112552, https://doi.org/10.1016/j.diamond.2025.112552.

23. E. M. Ahmed, H. Isawi, M. Morsy, M. H. Hemida, and H. Moustafa, "Effective Nanomembranes From Chitosan/PVA Blend Decorated Graphene Oxide With Gum Rosin and Silver Nanoparticles for Removal of Heavy Metals and Microbes From Water Resources," *Surfaces and Interfaces* 39 (2023): 102980, https://doi.org/10.1016/j.surfin.2023.102980.

24. H. Moustafa, M. A. Shemis, E. M. Ahmed, and H. Isawi, "Improvement of Hybrid Polyvinyl Chloride/Dapsone Membrane Using Synthesized Silver Nanoparticles for the Efficient Removal of Heavy Metals, Microorganisms, and Phosphate and Nitrate Compounds From Polluted Water," *RSC Advances* 14, no. 28 (2024): 19680–19700, https://doi.org/10.1039/D4RA03810J.

25. H. Isawi, E. M. Ahmed, M. Rabee, and H. Moustafa, "Using Natural Antioxidant Rhubarb Extracts in PVA/Chitosan Bio-Adsorbent Films for Efficient Removal of Cationic and Anionic Dyes From Polluted Water," *Journal of Industrial and Engineering Chemistry* 141 (2025): 626–644, https://doi.org/10.1016/j.jiec.2024.09.049.

26. X. Cui, H. Li, Z. Yao, et al., "Removal of Nitrate and Phosphate by Chitosan Composited Beads Derived From Crude Oil Refinery Waste: Sorption and Cost-Benefit Analysis," *Journal of Cleaner Production* 207 (2019): 846–856, https://doi.org/10.1016/j.jclepro.2018.10.027.

27. C. K. S. Pillai, W. Paul, and C. P. Sharma, "Chitin and Chitosan Polymers: Chemistry, Solubility and fiber Formation," *Progress in Polymer Science* 34, no. 7 (2009): 641–678, https://doi.org/10.1016/j.progpolymsci.2009.04.001.

28. S. B. Marpu and E. N. Benton, "Shining Light on Chitosan: A Review on the Usage of Chitosan for Photonics and Nanomaterials Research," *International Journal of Molecular Sciences* 19, no. 6 (2018): 1795, https://doi.org/10.3390/ijms19061795.

29. J. Wang, "Removal of Various Pollutants From Water and Wastewater by Modified Chitosan Adsorbents," *Critical Reviews in Environmental Science and Technology* 47 (2018): 1–56, https://doi.org/10.1080/10643389.2017.1421845.

30. T. Azzeddine, S. E. Marrane, O. Goudali, et al., "Simple and Modified Chitosan Gel Beads From a Natural Source as a Bio-Sorbent for Water Defluoridation: Experimental and Computational Perspectives," *Inorganic Chemistry Communications* 167 (2024): 112752, https://doi.org/10.1016/j.inoche.2024.112752.

31. L. S. Alqarni, J. S. Algethami, R. EL Kaim Billah, et al., "Synthesis and Characterization of a Crosslinked Deacetylated Chitin Modified Chicken Bone Waste-Derived Hydroxyapatite and TiO2 Biocomposite for Defluoridation of Drinking Water," *International Journal of Biological Macromolecules* 282 (2024): 136839, https://doi.org/10.1016/j.ijbiomac.2024.136839.

32. J. S. Algethami, R. Jugade, R. Billah El Kaim, et al., "Chitin Extraction From Crab Shells and Synthesis of Chitin @Metakaolin Composite for Efficient Amputation of Cr (VI) Ions," *Environmental Research* 252 (2024): 119065, https://doi.org/10.1016/j.envres.2024.119065.

33. J. S. Algethami, R. E. K. Billah, M. A. M. Alhamami, et al., "Confiscation of Cr(VI) by Cross-Linked Shrimp Waste-Derived Chitosan @ Al2O3 Nanocomposite: Experimental and Theoretical Approach," *Journal of Molecular Structure* 1321 (2025): 140182, https://doi.org/10.1016/j.molstruc.2024.140182.

34. B. G. K. Steiger and L. D. Wilson, "Modular Chitosan-Based Adsorbents for Tunable Uptake of Sulfate From Water," *International Journal of Molecular Sciences* 21, no. 19 (2020): 7130, https://doi.org/10.3390/ijms21197130.

35. J. Weißpflog, R. Boldt, B. Kohn, et al., "Investigation of Mechanisms for Simultaneous Adsorption of iron and Sulfate Ions Onto Chitosan With Formation of Orthorhombic Structures," *Colloids and Surfaces A: Physicochemical and Engineering Aspects* 592 (2020): 124575, https://doi.org/10.1016/j.colsurfa.2020.124575.

36. A. M. G. Mohamed, M. F. Mubarak, M. G. Snousy, et al., "Using Modified Clay-Chitosan Composite Filter as a Second Stage in the Conventional iron and Manganese Removal Plant System to Eliminate Permanent Hardness Anions in Drinkable Groundwater," *Environmental Advances* 13 (2023): 100407, https://doi.org/10.1016/j.envadv.2023.100407.

37. R. EL Kaim Billah, M. A. Khan, S. Essenni, et al., "A Mechanistic Insight Into Anionic Phosphate Adsorption on Developed Chitosan. ZnO@Metakaolin Biocomposite," *International Journal of Biological Macromolecules* 308 (2025): 142405, https://doi.org/10.1016/j.ijbiomac.2025.142405.

38. A. Manna, N. Naskar, K. Sen, and K. Banerjee, "A Review on Adsorption Mediated Phosphate Removal and Recovery by Biomatrices," *Journal of the Indian Chemical Society* 99, no. 10 (2022): 100682, https://doi.org/10.1016/j.jics.2022.100682.

39. Y. Liu, X. Zhang, and J. Wang, "A Critical Review of Various Adsorbents for Selective Removal of Nitrate From Water: Structure, Performance and Mechanism," *Chemosphere* 291 (2022): 132728, https://doi.org/10.1016/j.chemosphere.2021.132728.

40. Q. Zeng, I. Baker, J. Loudis, Y. Liao, and P. J. Hoopes, "Synthesis and Heating Effect of iron/iron Oxide Composite and iron Oxide Nanoparticles - Art. No. 64400H," *Proceedings of the Society of Photo-Optical*

Instrumentation Engineers 6440 (2007): 13, https://doi.org/10.1117/12.708182.

41. S. Pawar and A. Takke, "Regulatory Aspects, Types and Bioapplications of Metallic Nanoparticles: A Review," *Current Drug Delivery* 20, no. 7 (2023): 857–883, https://doi.org/10.2174/1567201819666220817110025.

42. S. Saqib, M. Farooq, H. Munis, et al., "Synthesis, Characterization and Use of iron Oxide Nano Particles for Antibacterial Activity," *Microscopy Research and Technique* 82 (2019): 415–420.

43. P. Karthikeyan and S. Meenakshi, "Fabrication of Hybrid Chitosan Encapsulated Magnetic-Kaolin Beads for Adsorption of Phosphate and Nitrate Ions From Aqueous Solutions," *International Journal of Biological Macromolecules* 168 (2021): 750–759, https://doi.org/10.1016/j.ijbiomac.2020.11.132.

44. L. Ding, C. Guo, Y. Zhu, et al., "Adsorptive Removal of Gallic Acid From Aqueous Solution Onto Magnetic Ion Exchange Resin," *Water Science and Technology* 81 (2020): 1479–1493, https://doi.org/10.2166/wst.2020.236.

45. N. Lambert, P. Van Aken, R. Van den Broeck, and R. Dewil, "Adsorption of Phosphate on iron-Coated Sand Granules as a Robust End-Of-Pipe Purification Strategy in the Horticulture Sector," *Chemosphere* 267 (2021): 129276, https://doi.org/10.1016/j.chemosphere.2020.129276.

46. Y. Zhan, J. Lin, and Z. Zhu, "Removal of Nitrate From Aqueous Solution Using Cetylpyridinium Bromide (CPB) Modified Zeolite as Adsorbent," *Journal of Hazardous Materials* 186, no. 2 (2011): 1972–1978, https://doi.org/10.1016/j.jhazmat.2010.12.090.

47. L. Jothinathan, G. Sozhan, and S. Vasudevan, "Recovery of Hydrogen and Removal of Nitrate From Water by Electrocoagulation Process," *Environmental Science and Pollution Research International* 20 (2013): 2184–2192, https://doi.org/10.1007/s11356-012-1028-4.

48. H. A. T. Banu, P. Karthikeyan, S. Vigneshwaran, and S. Meenakshi, "Adsorptive Performance of Lanthanum Encapsulated Biopolymer Chitosan-Kaolin Clay Hybrid Composite for the Recovery of Nitrate and Phosphate From Water," *International Journal of Biological Macromolecules* 154 (2020): 188–197, https://doi.org/10.1016/j.ijbiomac.2020.03.074.

49. H. Qiu, L. Lv, C. Pan, Q. Zhang, W. m. Zhang, and Q. x. Zhang, "Critical Review in Adsorption Kinetic Models," *Journal of Zhejiang University. Science. A* 10 (2009): 716–724, https://doi.org/10.1631/jzus.A0820524.

50. J. Wang and X. Guo, "Adsorption Kinetic Models: Physical Meanings, Applications, and Solving Methods," *Journal of Hazardous Materials* 390 (2020): 122156, https://doi.org/10.1016/j.jhazmat.2020.122156.

51. Q. Hu, N. Chen, C. Feng, J. Zhang, W. Hu, and L. Lv, "Kinetic Studies of Nitrate Removal From Aqueous Solution Using Granular Chitosan-Fe(III) Complex," *Water Science and Technology* 73, no. 5 (2015): 1211–1220, https://doi.org/10.2166/wst.2015.596.

52. Z. Takai, M. Mustafa, S. Asman, and K. Sekak, "Preparation and Characterization of Magnetite (Fe3O4) Nanoparticles by sol-Gel Method," *International Journal Of Nanoelectronics And Materials* 12 (2019): 37–46.

53. A. Hussain, A. Jadhav, Y. K. Baek, H. Choi, J. Lee, and Y. Kang, "One Pot Synthesis of Exchange Coupled Nd2Fe14B/Alpha-Fe by Pechini Type sol-Gel Method," *Journal of Nanoscience and Nanotechnology* 13 (2013): 7717–7722, https://doi.org/10.1166/jnn.2013.7833.

54. R. P. Gambhir, A. K. Parthasarathy, S. Sharma, S. Kale, V. V. Magdum, and A. P. Tiwari, "pH-Responsive glycine Functionalized Magnetic iron Oxide Nanoparticles for SARS-CoV-2 RNA Extraction From Clinical Sample," *Journal of Materials Science* 57, no. 28 (2022): 13620–13631, https://doi.org/10.1007/s10853-022-07464-6.

55. J. Xu, H. Yang, W. Fu, et al., "Preparation and Magnetic Properties of Magnetite Nanoparticles by Sol–Gel Method," *Journal of Magnetism and Magnetic Materials* 309, no. 2 (2007): 307–311, https://doi.org/10.1016/j.jmmm.2006.07.037.

56. Y. h. Zheng, Y. Cheng, F. Bao, and Y. s. Wang, "Synthesis and Magnetic Properties of Fe3O4 Nanoparticles," *Materials Research Bulletin* 41, no. 3 (2006): 525–529, https://doi.org/10.1016/j.materresbull.2005.09.015.

57. S. V. Durán, B. Lapo, M. Meneses, and A. M. Sastre, "Recovery of Neodymium (III) From Aqueous Phase by Chitosan-Manganese-Ferrite Magnetic Beads," *Nanomaterials* 10, no. 6 (2020): 1204, https://doi.org/10.3390/nano10061204.

58. G. L. Rorrer, T. Y. Hsien, and J. D. Way, "Synthesis of Porous-Magnetic Chitosan Beads for Removal of Cadmium Ions From Wastewater," *Industrial and Engineering Chemistry Research* 32, no. 9 (1993): 2170–2178, https://doi.org/10.1021/ie00021a042.

59. N. N. Nassar, "Rapid Removal and Recovery of pb(II) From Wastewater by Magnetic Nanoadsorbents," *Journal of Hazardous Materials* 184, no. 1 (2010): 538–546, https://doi.org/10.1016/j.jhazmat.2010.08.069.

60. Y. Cengeloglu, A. Tor, M. Ersoz, and G. Arslan, "Removal of Nitrate From Aqueous Solution by Using Red Mud," *Separation and Purification Technology* 51, no. 3 (2006): 374–378, https://doi.org/10.1016/j.seppur.2006.02.020.

61. E. Mohammadi, H. Daraei, R. Ghanbari, et al., "Synthesis of Carboxylated Chitosan Modified With Ferromagnetic Nanoparticles for Adsorptive Removal of Fluoride, Nitrate, and Phosphate Anions From Aqueous Solutions," *Journal of Molecular Liquids* 273 (2019): 116–124, https://doi.org/10.1016/j.molliq.2018.10.019.

62. H. Ao, W. Cao, Y. Hong, J. Wu, and L. Wei, "Adsorption of Sulfate Ion From Water by Zirconium Oxide-Modified Biochar Derived From Pomelo Peel," *Science of the Total Environment* 708 (2020): 135092, https://doi.org/10.1016/j.scitotenv.2019.135092.

63. Y. Chen and J. Wang, "Removal of Radionuclide Sr2+ Ions From Aqueous Solution Using Synthesized Magnetic Chitosan Beads," *Nuclear Engineering and Design* 242 (2012): 445–451, https://doi.org/10.1016/j.nucengdes.2011.10.059.

64. T. Dong, "Nitrogen Removal From Groundwater Using Scoria: Kinetics, Equilibria and Microstructure," *Journal of Environmental Science and Health, Part A: Toxic/Hazardous Substances & Environmental Engineering* 56 (2021): 1–8, https://doi.org/10.1080/10934529.2021.1883958.

65. C. F. Chang, C. Y. Chang, and T. L. Hsu, "Removal of Fluoride From Aqueous Solution With the Superparamagnetic Zirconia Material," *Desalination* 279, no. 1 (2011): 375–382, https://doi.org/10.1016/j.desal.2011.06.039.

66. Z. Yu, X. Zhang, and Y. Huang, "Magnetic Chitosan–Iron(III) Hydrogel as a Fast and Reusable Adsorbent for Chromium(VI) Removal," *Industrial and Engineering Chemistry Research* 52, no. 34 (2013): 11956–11966, https://doi.org/10.1021/ie400781n.

67. A. S. Eltaweil, K. Ibrahim, E. M. Abd El-Monaem, G. M. El-Subruiti, and A. M. Omer, "Phosphate Removal by Lanthanum-Doped Aminated Graphene Oxide@Aminated Chitosan Microspheres: Insights Into the Adsorption Mechanism," *Journal of Cleaner Production* 385 (2023): 135640, https://doi.org/10.1016/j.jclepro.2022.135640.

68. H. V. Tran, L. D. Tran, and T. N. Nguyen, "Preparation of Chitosan/Magnetite Composite Beads and Their Application for Removal of pb(II) and Ni(II) From Aqueous Solution," *Materials Science and Engineering: C* 30, no. 2 (2010): 304–310, https://doi.org/10.1016/j.msec.2009.11.008.

69. E. El-Monaem, M. Salah Ayoup, A. Omer, E. Hammad, and A. Eltaweil, "Sandwich-Like Construction of a New Aminated Chitosan Schiff Base for Efficient Removal of Congo Red," *Applied Water Science* 13 (2023): 67, https://doi.org/10.1007/s13201-023-01866-w.

70. J. Kiefer, A. Stärk, A. Kiefer, and H. Glade, "Infrared Spectroscopic Analysis of the Inorganic Deposits From Water in Domestic and Technical Heat Exchangers," *Energies* 11 (2018): 798, https://doi.org/10.3390/en11040798.

71. Y. S. Vidya and B. N. Lakshminarasappa, "Preparation, Characterization, and Luminescence Properties of Orthorhombic Sodium Sulphate," *Physics Research International* 2013 (2013): 641631, https://doi.org/10.1155/2013/641631.

72. A. Periasamy, S. Muruganand, and M. Palaniswamy, "Vibrational Studies of Na2so4, K2so 4, NaHSO4and KHSO4 Crystals," *Rasayan Journal of Chemistry* 2 (2009): 981–989.

73. S. Hong, F. S. Cannon, P. Hou, T. Byrne, and C. Nieto-Delgado, "Adsorptive Removal of Sulfate From Acid Mine Drainage by Polypyrrole Modified Activated Carbons: Effects of Polypyrrole Deposition Protocols and Activated Carbon Source," *Chemosphere* 184 (2017): 429–437, https://doi.org/10.1016/j.chemosphere.2017.06.019.

74. C. Pizarro, M. Escudey, C. Bravo, M. Gacitua, and L. Pavez, "Sulfate Kinetics and Adsorption Studies on a Zeolite/Polyammonium Cation Composite for Environmental Remediation," *Minerals* 11 (2021): 180, https://doi.org/10.3390/min11020180.

Supporting Information

Additional supporting information can be found online in the Supporting Information section. **Table S1:** Experimental data set for batch adsorption removal of sulfate using IOICBs. (Conditions: Temperature = 25°C, Solution volume = 30 mL, Surface area = 0.3255 m^2/g). **Table S2:** Descriptive statistical analysis of experimental data set for adsorption removal of sulfate using IOICBs. **Figure S1:** Normal distribution of data set count from experimental parameters versus adsorption capacity (Qe) for sulfate removal using IOICBs. **Figure S2:** Pearson correlation heatmap between input experimental parameters and output parameter adsorption capacity. **Figure S3:** XRD analysis of neat chitosan.